

Ice formation in Saharan dust over central Europe observed with temperature/humidity/aerosol Raman lidar

Albert Ansmann, Ina Mattis, Detlef Müller, Ulla Wandinger, Marcus Radlach, and Dietrich Althausen

Leibniz Institute for Tropospheric Research, Leipzig, Germany

Richard Damoah

Abteilung für Ökologie, Technische Universität München, Freising-Weihenstephan, Germany

Received 11 May 2004; revised 17 August 2004; accepted 17 August 2004; published 26 April 2005.

[1] Three gravity-wave-induced clouds and a glaciating altocumulus layer were continuously monitored with lidar at Leipzig, Germany, on 21 November 2003. The midtropospheric clouds formed in Saharan dust at heights from 3.5 km (-9°C) to 6.5 km (-27°C). Distinct ice formation in the altocumulus was triggered by the gravity wave. For the first time, an aerosol/cloud study presents height profiles of temperature, water vapor mixing ratio, relative humidity, dust, and cloud optical properties (volume extinction and backscatter coefficients, lidar ratio, depolarization ratio) within the same air column, solely derived from lidar data. The three gravity-wave-induced clouds did not show any sign of ice formation. The aged dust particles below 4.5-km height were probably partly coated and mixed with hygroscopic material and thus deactivated concerning ice nucleation. Ice crystals were generated in isolated air parcels at the cloud edges of a young, optically thin altocumulus layer between 5- and 6.5-km height. An aged altocumulus deck composed of a geometrically thin liquid water layer at cloud top and an extended ice crystal layer (ice virga) was observed 2 hours later in the same height range. Strong ice formation occurred in the altocumulus during the downdraft induced by the gravity wave. Contact freezing was probably the main reason for the observed ice formation on dust particles. Ice depolarization ratios were relatively low with values from 10 to 15% in the altocumulus and indicate plate-like crystals.

Citation: Ansmann, A., I. Mattis, D. Müller, U. Wandinger, M. Radlach, D. Althausen, and R. Damoah (2005), Ice formation in Saharan dust over central Europe observed with temperature/humidity/aerosol Raman lidar, *J. Geophys. Res.*, *110*, D18S12, doi:10.1029/2004JD005000.

1. Introduction

[2] We observed gravity-wave-induced clouds at temperatures from -9 to -16°C and glaciating altocumulus clouds at temperatures from -18 to -27°C in a Saharan dust layer that extended from the boundary layer top to about 8- to 9-km height. The continuous lidar observations provide the unique opportunity to study the potential of aged desert dust particles initiating ice particle formation (deposition, condensation, immersion, contact freezing [Pruppacher and Klett, 1997]) under comparably warm conditions at temperatures above -30°C . The usually dominating process of homogeneous freezing of supercooled cloud drops needs temperatures below about -35°C [DeMott *et al.*, 1997; Sassen and Benson, 2000].

[3] In a recent field campaign in southern Florida, Sassen *et al.* [2003] observed that Saharan dust particles are effective ice nuclei, apparently capable of glaciating a mildly supercooled (-5.2 to -8.8°C) altocumulus cloud.

Clay materials (kaolinite, montmorillonite) have been found to be active ice nuclei (IN) [Mason and Maybank, 1958; Isono *et al.*, 1959; Mason, 1960; Hoffer, 1961] initiating the formation of ice crystals at temperatures as high as -4 to -14°C [Roberts and Hallett, 1968; Pitter and Pruppacher, 1973; Schaller and Fukuta, 1979; Pruppacher and Klett, 1997]. The great efficacy of some dust particles to serve as IN has been attributed to crystallographic similarities of the dust particles with ice. The Florida results of Sassen *et al.* [2003] for Saharan dust were similar to those for Asian dust storm particles observed over the western US [Sassen, 2002]. Case studies of cirrus clouds and climatology-based comparisons of cirrus observations in dust layers and dust-free air showed that ice clouds may already form at moderate temperatures about 20 K higher than what is typical under background (sulfate) aerosol conditions in the middle and upper troposphere. Sakai *et al.* [2004] reported on a cirrus layer that was formed in an optically dense Asian desert dust plume at temperatures of -19 to -35°C . All these findings are in agreement with laboratory studies of Zuberi *et al.* [2002]. Their results showed that mineral dust causes aqueous $(\text{NH}_4)_2\text{SO}_4\text{-H}_2\text{O}$ particles to

freeze at temperatures 8–20 K higher than the temperatures at which drops without immersions of insoluble mineral dust particles normally start to freeze. Thus dust storms in the northern hemisphere may play a role in modulating climate through the indirect aerosol effect on cloud properties so that even minor changes in human-induced land use leading to desertification may have a sensitive effect on regional weather and global climate [Sassen *et al.*, 2003; Tegen *et al.*, 2004].

[4] Laboratory studies dealing with ice nucleation on dust have been undertaken since the 1950s. The different ice formation mechanisms have been identified and studied in detail since then. They are summarized in section 3. However, atmospheric measurements are scarce [DeMott, 2002]. Atmospheric observations of the relative importance of the different freezing mechanisms under given environmental temperature, moisture, and dust conditions are not available. No attempt has been made so far to investigate the role of pure and aged dust or mixed (dust/anthropogenic/maritime) aerosols in atmospheric cloud formation.

[5] Lidar is very useful for dust-related cloud studies because both height profiles of dust parameters as well as of cloud optical properties can be continuously monitored. In the case of the Raman lidar used here, meteorological state parameters were measured in addition. The lidar permits the simultaneous determination of vertical profiles of air temperature, water-vapor-to-dry-air-mixing ratio, and thus of relative humidity, and aerosol and cloud optical properties, i.e., backscatter coefficients at 355, 532, and 1064 nm, extinction coefficients at 355 and 532 nm, lidar ratios (extinction to backscatter ratios) at 355 and 532 nm, and depolarization ratio at 532 nm. The depolarization ratio (in combination with the lidar ratio) is rather important to distinguish between anthropogenic particle plumes and desert dust layers, and between liquid particles (spheres) and nonspherical ice crystals [Sassen, 1991; Reichardt *et al.*, 2002; Sakai *et al.*, 2003; Mattis *et al.*, 2002b]. It is important to note that for the first time relative humidity profiles solely determined from lidar data are used in a cloud study. In contrast to radiosondes, lidars allow us to measure humidity profiles with high temporal resolution and, what is most important, in the same air parcel in which the dust and cloud optical properties are measured.

[6] The observation presented here was taken at Leipzig (52°N, 12°E), Germany, on 21 November 2003. The Raman lidar is part of the European Aerosol Research Lidar Network (EARLINET, [Bösenberg *et al.*, 2003; Ansmann *et al.*, 2003]) and routinely measures tropospheric aerosol profiles since 1997 [Mattis, 2002; Mattis *et al.*, 2004]. Dust outbreaks can be monitored 5–15 times per year over central Europe and in almost 80% of these events a mixture of clouds and dust is observed. In section 2, the lidar and the data analysis methods are briefly described. Section 3 provides a short overview of the ice formation mechanisms relevant to our observations. The lidar measurements are discussed in detail in section 4. Concluding remarks are given in section 5.

2. Instrument and Data Analysis

[7] A full description of the system is given by Mattis *et al.* [2002a]. A Nd:YAG laser emits pulses at 355 nm (200 mJ),

532 nm (500 mJ), and 1064 nm (500 mJ) simultaneously. Laser shots are fired with a repetition rate of 30 Hz. A 1-m-diameter Cassegrain telescope collects radiation backscattered by atmospheric molecules and particles. Elastically backscattered lidar signals at the three laser wavelengths and signals within the vibrational-rotational Raman band of nitrogen at 387 and 607 nm and of water vapor at 408 nm (excited by radiation at 355 and 532 nm) are separated with dichroic mirrors and interference filters. Water vapor Raman signals are only detectable at nighttime. Rotational Raman signals measured at 532-nm laser wavelength are separated by the use of a double grating monochromator. Rotational Raman backscatter signals are detected under daytime conditions with a Fabry Perot interferometer that suppresses sky background light [Arshinov *et al.*, 2001; Bobrovnikov *et al.*, 2002]. Linearly polarized laser light is transmitted at 532 nm, and the parallel- (with respect to the polarization of the laser light) and cross-polarized returns are detected by the use of a polarization-sensitive beam splitter. All signals are recorded with photomultiplier tubes in the photon-counting mode and stored with temporal and vertical resolution of 30 s and 60 m, respectively.

[8] Well-known Raman lidar methods are applied to determine temperature, water vapor, and relative humidity [Mattis *et al.*, 2002a] and particle optical properties [Ansmann *et al.*, 1990, 1992; Ansmann, 2002; Müller *et al.*, 2003]. An Ångström exponent of zero for dust and cloud extinction coefficients is used in the retrieval of the extinction profiles from the nitrogen Raman signals. All cloud signals were checked for detector overload effects.

[9] Air mass transport is characterized on the basis of height-resolved backward trajectories that were calculated with the three-dimensional trajectory model FLEXTRA [Stohl *et al.*, 1995]. Global model level wind fields of the spectral model T511 L60 of the *European Centre for Medium-Range Weather Forecasts (ECMWF)* [1995] were used as input for FLEXTRA.

3. Ice Formation Mechanisms

[10] Four different ice formation mechanisms are relevant to our observations. According to laboratory studies, condensation freezing on clay particles occurs when the air is water supersaturated (and thus also ice supersaturated), temperatures are below about -10 to -11°C and ice supersaturation is above 12% [Roberts and Hallett, 1968; Schaller and Fukuta, 1979]. Clay particles are fully activated if temperatures are below -28°C [Pitter and Pruppacher, 1973]. The soluble particle component causes condensation and the insoluble component catalyzes freezing instantaneously [DeMott, 2002]. The nucleation process is referred to as immersion freezing if the insoluble component catalyzes ice formation at a much later time (at lower temperatures or greater droplet dilution [DeMott *et al.*, 1997; DeMott, 2002; Zuberi *et al.*, 2002]).

[11] When the air is only supersaturated with respect to ice and thus water subsaturated, the third mechanism called deposition freezing (direct deposition of ice to an insoluble surface) takes place. Here the temperatures must fall below a critical value of -18 to -19°C , and a critical ice supersaturation value of 20% must be surpassed [Roberts and Hallett, 1968; Schaller and Fukuta, 1979].

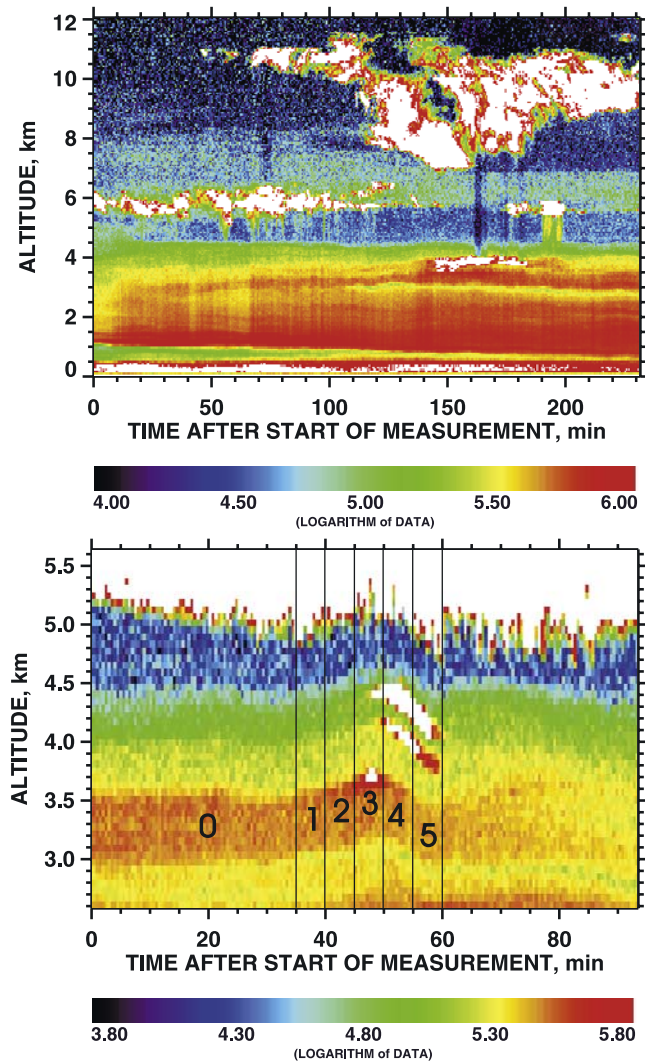


Figure 1. Range-corrected 1064-nm signal measured at Leipzig, Germany, on 21 November 2003, (top) 1212–1600 UTC (afternoon), and (bottom) 1627–1800 UTC (evening). Green to red indicate dust. Clear air is indicated by dark blue. Clouds (white) were present at heights above 3.5 km. A gravity wave crossed the lidar site in the evening and caused the formation of three clouds in the dust. Vertical stripes in Figure 1 (top), especially below the 6-km cloud layer, are artifacts (caused by 1064-nm detector problems). Time intervals 0–5 are defined and indicated by vertical lines in Figure 1 (bottom). Lidar results for these periods are discussed in section 4.2.

[12] According to the fourth mechanism, the contact freezing mechanism, dust particles can initiate ice phase at the moment of their contact with the supercooled drops. Kaolinite particles become activated in this way at -4°C and are fully activated at temperatures around -14°C [Pitter and Pruppacher, 1973; Pruppacher and Klett, 1997].

4. Observations

[13] In section 4.1 we begin with an overview of the dust and cloud optical properties and the meteorological conditions on 21 November 2003. The cloud observations are

then discussed in detail in sections 4.2–4.3 with focus on ice formation, starting with the warmest clouds, i.e., the gravity-wave-induced clouds (section 4.2), followed by the altocumulus observations in the afternoon and in the evening of 21 November (section 4.3).

4.1. Dust and Cloud Optical Properties and Meteorological Conditions

[14] As a result of a Saharan dust outbreak, layers of desert dust crossed the Mediterranean Sea, southern and eastern France and reached central Europe on 21 November 2003. Figure 1 provides an overview of the observations at Leipzig, Germany. Figure 2 shows backward trajectories calculated for Leipzig, 1300 UTC arrival time. Figures 3 and 4 present 35–60 min average profiles of dust and cloud optical properties and meteorological state parameters.

[15] Two distinct dust layers were observed (see Figure 1). An optically dense dust layer extended from 0.5- to 1-km to 4.5-km height, whereas an optically thin layer was found between 5.5- and 8-km height. Traces of dust were present even above 8-km height. According to the backward trajectories in Figure 2 the lower layer crossed the Mediterranean Sea and southern Europe at low heights during the last 3 days before it arrived at the lidar site. Dust particles were presumably mixed with maritime and urban aerosols and partly coated with hygroscopic material as a result of coagulation with Aitken particles or adsorption of gases such as SO_2 . The dust layer observed above 5.5-km height crossed anthropogenically polluted areas at comparably high altitudes and thus was most probably less contaminated by aerosol pollution. The backward trajectory arriving at 5-km height (550 hPa, not shown in Figure 2) shows no sign of dust uptake. The respective air mass was always above the 600-hPa level (above 4.2-km height) during the 8-day travel.

[16] The volume extinction coefficients of $40\text{--}80\text{ Mm}^{-1}$ (see Figures 3 and 4) below 4-km height are typical for moderate Saharan dust outbreaks. During major outbreaks we observed values up to $300\text{--}500\text{ Mm}^{-1}$ over central and

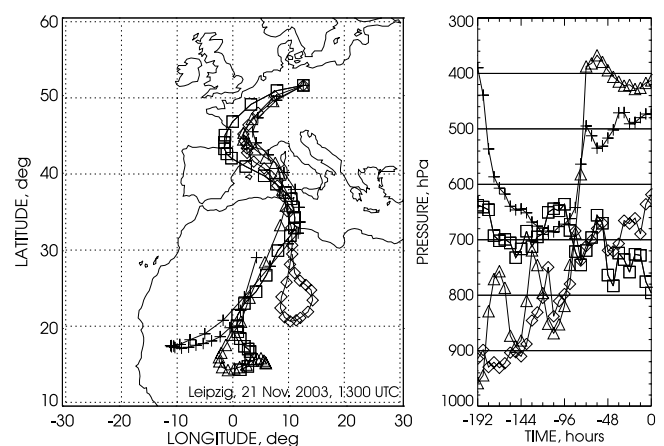


Figure 2. Eight-day backward trajectories arriving over Leipzig, Germany, on 21 November 2003, 1300 UTC. Arrival heights are 2 km (795 hPa, squares), 4 km (620 hPa, diamonds), 6 km (475 hPa, crosses), and 7 km (410 hPa, triangles). The time step between individual symbols is 6 hours. Dust-laden air left Africa about 60–80 hours before arriving over Leipzig.

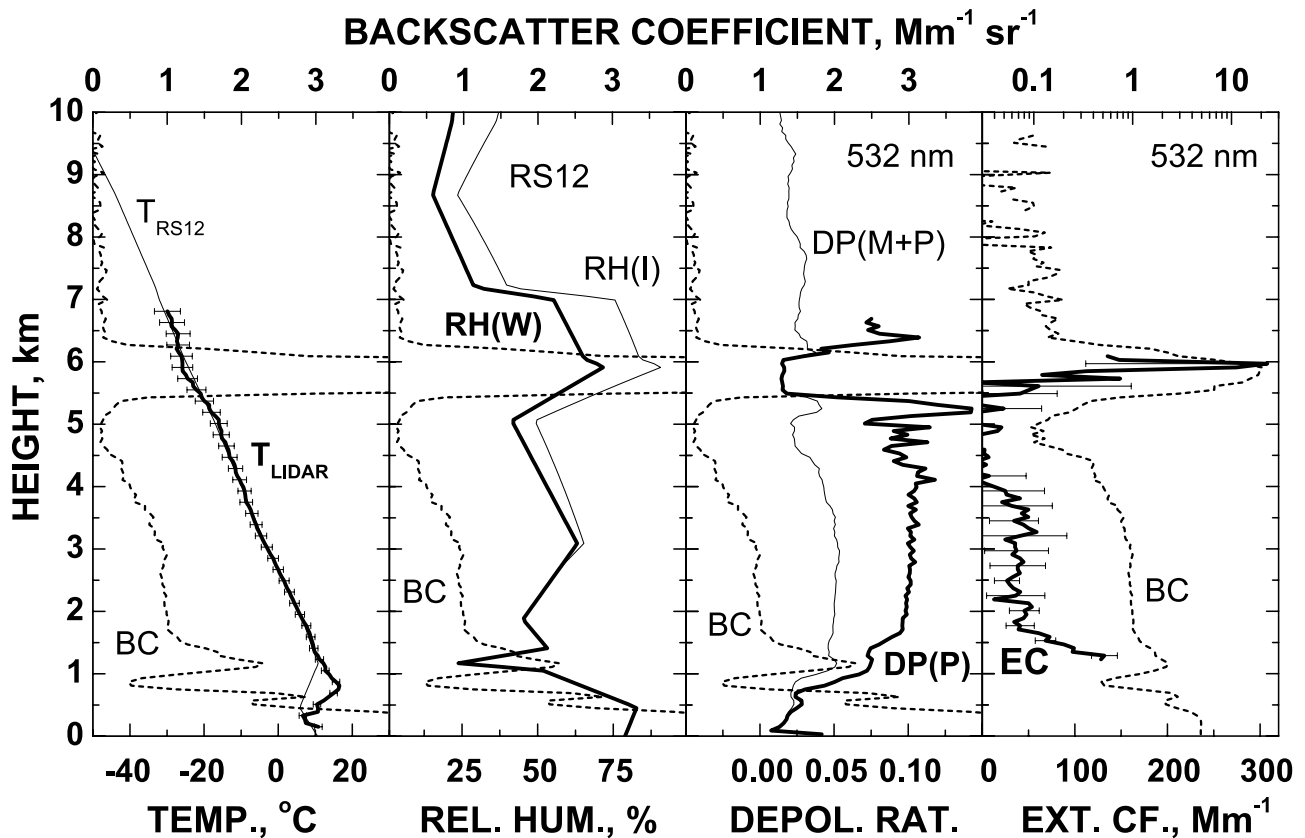


Figure 3. One-hour mean lidar profiles (1212–1312 UTC, first hour in Figure 1, afternoon) of temperature (thick line), total (molecule plus particle) depolarization ratio (DP(M+P), thin line), particle depolarization ratio (DP(P), thick line), and particle extinction coefficient (EC, 532 nm, thick line). Backscatter coefficient (BC, 532 nm, dashed line) indicates the dust layer and the altocumulus layer. Error bars (standard deviation) include statistical and systematic errors. Lidar profiles are smoothed with window lengths of 300 m (temperature, below 1500-m height), 2000 m (temperature above 2000-m height), and 600 m (extinction coefficient). Radiosonde profiles (RS12, launched at Oppin, 35 km northwest of Leipzig at 1200 UTC) of temperature (thin line) and of relative humidity (RH(W) relative humidity over water (thick line), RH(I) relative humidity over ice (thin line)) are shown in addition.

northern parts of Europe [Ansmann *et al.*, 2003]. Unfortunately, the dust extinction coefficients could only be determined with good accuracy below the altocumulus deck and hence only in the dense dust layer. However, from the backscatter coefficients we estimate that the dust extinction coefficients in the upper dust layer were about 5–15 Mm^{-1} .

[17] It is worth mentioning that the extinction coefficients in Figure 3 are determined from the rotational Raman signals. As already shown by Müller *et al.* [2003], aerosol Raman lidar observations at 355 and 532 nm are no longer restricted to nighttime hours.

[18] The particle depolarization ratios of 0.1–0.12 above 2-km height were about a factor of two lower than values we typically observe in dust after long-range transport [Müller *et al.*, 2003]. The particle depolarization ratio is calculated from the total (molecule plus particle) depolarization ratio and becomes very noisy (and is thus not shown) when the particle backscatter coefficient is close to zero. The low particle depolarization ratios as well as the comparably low dust lidar ratios of around 50 sr in Figure 4 corroborate our assumption that we observed an aged dust plume with a mixture of sea salt, anthropogenic aerosols,

coated and pure dust particles. In pure Saharan dust (not perturbed by maritime and anthropogenic particles and gases) we found much higher lidar ratios of 60–90 sr [Mattis *et al.*, 2002b] and particle depolarization ratios close to 0.25 [Müller *et al.*, 2003]. The good correlation of the backscatter coefficient with relative humidity at relative humidities above 60% in Figure 4 also reflects the presence of hygroscopic particles in the lower dust layer.

[19] In a previous study based on multiwavelength lidar and Sun photometer observations [Müller *et al.*, 2003] we found that the effective radius of dust particles after long-range transport to central Europe was 0.3–0.7 μm . Large particles with radius of $>1 \mu\text{m}$ were widely absent.

[20] Broken altocumulus fields appeared in the lower part of the upper dust layer (see Figure 1, afternoon). A radiosonde launched 35 km northwest of Leipzig at 1200 UTC indicated a moist layer from 5.8- to 7-km height (see Figure 3). Temperatures ranged from -18 to -27°C in the cloudy layer. The 1-hour mean extinction coefficients of up to 300 Mm^{-1} in the cloudy region (mixture of broken clouds and dust) indicate that the clouds were optically thin with 532-nm optical depth mainly

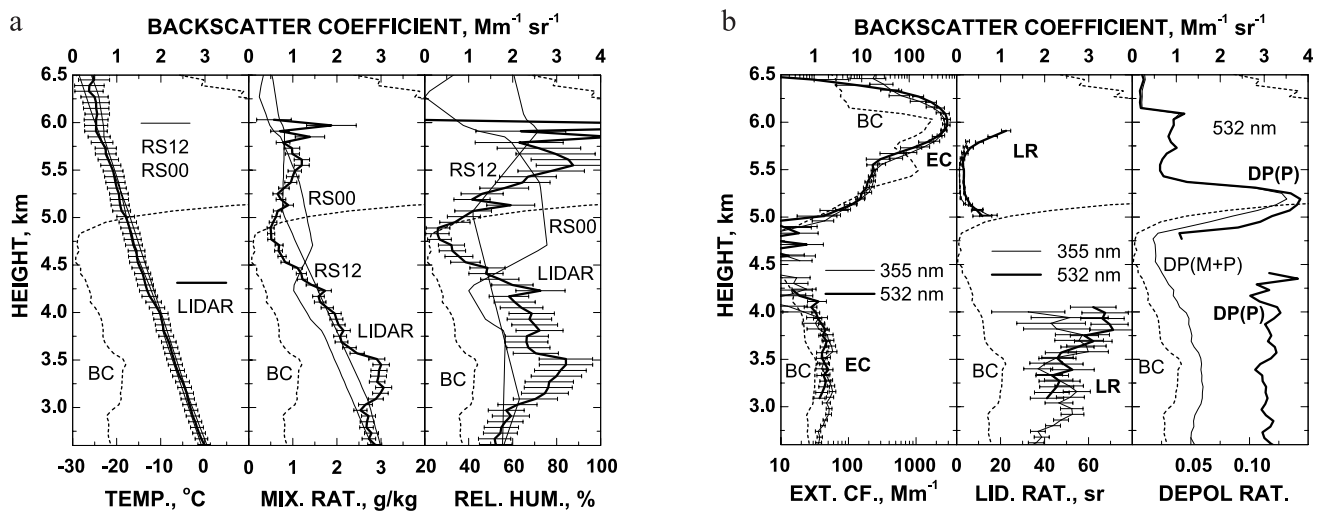


Figure 4. (a) Meteorological state parameters and (b) dust optical properties observed with Raman lidar on 21 November 2003, 1627–1702 UTC (35-min average, time period 0 in Figure 1, evening). Radiosonde temperature and humidity profiles of 21 November, 1200 UTC (RS12), and 22 November, 0000 UTC (RS00), are shown for comparison (Figure 4a). LR denotes lidar ratio. Relative humidity is calculated from the mixing ratio and the saturation mixing ratio as a function of the lidar-derived temperature. Signal smoothing lengths are 600 m (extinction, lidar ratio) and 2000 m (temperature). Error bars include signal noise and uncertainties of the input parameters used in the retrieval.

below 0.5. From the peak extinction coefficients of 200–300 Mm^{-1} (600-m signal smoothing) and the peak backscatter coefficients of 10–15 $\text{Mm}^{-1} \text{sr}^{-1}$ (600-m signal smoothing, in Figure 3 the resolution is 60 m) we obtain typical water-cloud lidar ratios around 20 sr [O'Connor *et al.*, 2004]. Depolarization ratios were close to zero (0.02) in the cloud center region and also indicate drops. Depolarization peaks just below and above the main cloud region were caused by ice crystals as will be discussed in section 4.3.

[21] An aged, well-developed altocumulus deck was observed in the evening. In Figure 4, backscatter coefficients show a well-defined cloud top at 6150 m. A liquid water layer of 100- to 200-m depth was present at cloud top. In this layer, the particle extinction coefficients reached maximum values of 2700 Mm^{-1} (Figure 4, 600-m signal smoothing) and 5000 Mm^{-1} (5 km^{-1}) in the case of 180-m signal smoothing. Such high extinction coefficients in rather thin layers indicate liquid water drops [Hogan *et al.*, 2003b]. The 532-nm optical depth of the thin layer was close to one. The 532-nm lidar ratio, calculated from lidar signals smoothed with 180-m window length, was 18.2 sr and again indicates drops. In the lower part of the altocumulus the extinction coefficients were an order of magnitude lower. The optical depth was close to 0.2 for the 5- to 5.8-km height range. Very low lidar ratios around 2 sr in the central part of the cloud layer indicate falling, horizontally aligned ice crystals [Ansmann *et al.*, 1992; Reichardt *et al.*, 2002]. Horizontally oriented ice crystals cause specular reflection (very large backscatter coefficients). The depolarization ratio in Figure 4, averaged over 35 min, reflects the presence of ice crystals at the base of the cloud deck and ice crystals as well as drops in the upper part of the cloud system. When comparing the backscatter and depolarization profiles with the extinction and lidar ratio profiles in

Figure 4, the different effective resolutions (60 m versus 600 m) should be kept in mind. The humidity profiles suggest that the air was water subsaturated throughout the altocumulus except for the uppermost liquid water layer. The high optical depth close to cloud top prohibited a trustworthy detection of the water vapor Raman signal in the liquid water layer. The altocumulus observation is further discussed in section 4.3.

[22] A cirrus deck extended from 7 km up to the tropopause during the afternoon observation. Temperatures ranged from -32 to -61°C in the 7- to 11-km height range. After the passage of a thick ice crystal virga, the dust appears to be removed (scavenged) by the ice particles at heights below about 9 km (see Figure 1, afternoon). However, in agreement with the backward trajectories, it is more likely that the air mass transport pattern changed with time in the upper troposphere. According to the backward trajectories, the cirrus formed in dust-free air and the ice crystal virga and subsequent clean air masses above 7-km height crossed the field site from the west while the dust was transported from southwest.

[23] Five gravity waves crossed eastern Germany between 1600 and 2200 UTC on 21 November 2003, according to surface pressure observations at the Leipzig lidar site and the Lindenberg Meteorological Observatory (MOL) 180 km northeast of Leipzig. The most pronounced wave (surface pressure amplitude of about 0.2 hPa) was observed between 1700 and 1800 UTC (see Figure 1, evening). The wave crest crossed Leipzig at 1720 UTC and MOL 15 min later. According to surface pressure observations at five sites within an area of 5 km \times 5 km around MOL, this gravity wave moved to the southeast, and had a wavelength of 25–30 km, a wave period of 65–75 min, and phase speed of 6–7 m/s. In the determination of the wave parameters southwesterly winds and mean wind speeds of

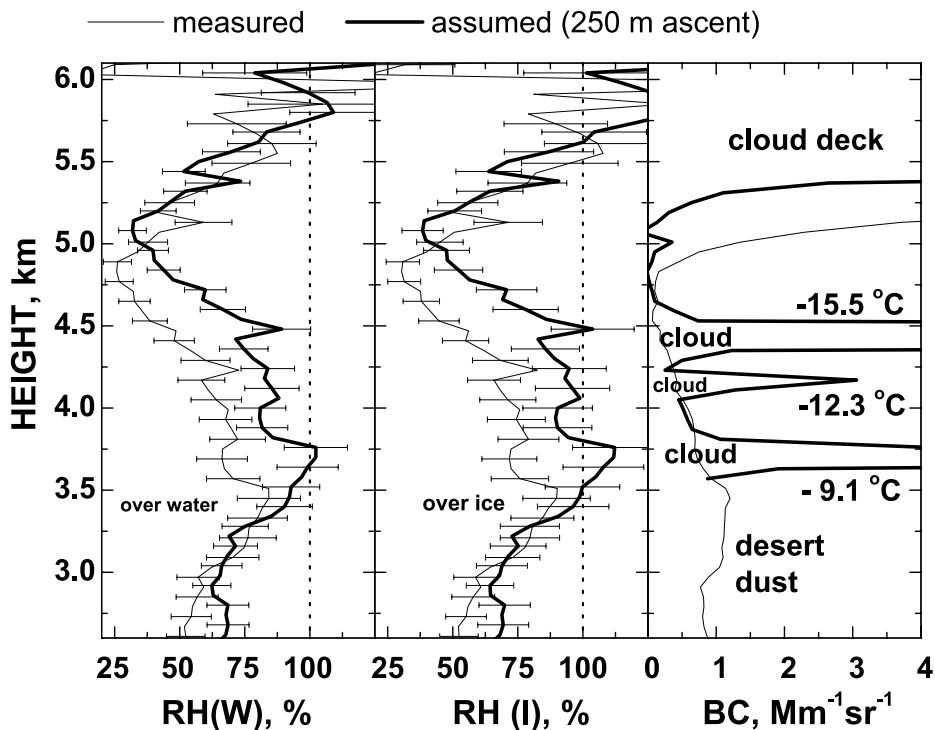


Figure 5. Measured (thin lines, before ascent) and estimated (thick lines) relative humidity profiles after lifting of the air column by 250 m. RH(W) and RH(I) denote relative humidity with respect to water and ice, respectively. The backscatter coefficients (BC) show the desert dust layer before the arrival of the gravity wave and a composite picture that indicates the cloud layers. The vertical shift of the cloud deck above 5-km height clearly indicates the lifting by 250 m. Cloud center temperatures are given in addition.

15–20 km (measured with radiosondes in the free troposphere at Oppin and at MOL between 1200 and 2400 UTC) were taken into account. This strong gravity wave led to the formation of three clouds within a moist layer in the dust at heights of 3.7 km (-9°C), 4.1 km (-12°C), and 4.4 km (-15.5°C) and also disturbed the evolution of the altocumulus deck and triggered ice formation as discussed in section 4.3.

[24] Vector analysis on the basis of the determined wave characteristics (from the five-point observations) and the radiosonde wind field information yields an observed apparent wavelength, period and phase velocity (along the wind direction) of 35–45 km, 30 min, and 20–25 m/s over the lidar site, respectively. The air parcels passed through the gravity wave with a relative speed of about 5 m/s (15–20 m/s wind velocity minus 20–25 m/s apparent wave phase velocity) and thus experienced the wave (up and downward motions) for about 120 to 150 min. The clouds appeared after lifting of the air by 250 m. The ascent rate of 0.1–0.15 m/s was estimated from the slope of the wave (ratio of the vertical wave amplitude (250 m) to the horizontal scale (9–11 km, one fourth of the apparent wavelength) multiplied by the relative wave propagation speed of 5 m/s.

4.2. Gravity-Wave-Induced Clouds

[25] We begin the analysis with the study of the humidity conditions during cloud formation. Because accurate lidar measurements of relative humidity (RH) were only possible with a temporal resolution (signal averaging) of 30–60 min,

we made two attempts to estimate the RH profile for the time periods 3 and 4 in Figure 1 (evening). In the first approach we started with the RH profile measured during period 0 in Figure 1. This profile is shown in Figure 4 and also in Figure 5 (thin line). We assumed (1) adiabatic cooling during the lifting of the air parcels by 250 m, (2) that the mixing ratio determined before the arrival of the gravity wave (time period 0) represents the humidity conditions at the beginning of time period 1, and (3) that the shape of the height profile of the water vapor mixing ratio remained undisturbed during the lifting process (over the time periods 1–3 in Figure 1). The resulting relative humidity profile is shown in Figure 5. As can be seen, the cloud at 3.7-km height appeared when 100% relative humidity with respect to water was reached. In the case of the other two clouds the lidar data indicate ice saturation only.

[26] We made a further attempt to estimate the humidity conditions during cloud formation. Our second estimation is based on measured 5-min mean mixing ratio profiles (periods 1–5 in Figure 1). These profiles can be determined with a tolerable uncertainty of $<10\%$ if the Raman signals are smoothed with window lengths of 180 m. The respective 5-min mean temperature profiles were, however, too noisy for direct calculations of RH, but indicated the general trend of the temperature development during the passage of the gravity wave. As can be seen in Figure 6, the 5-min temperatures show a cooling in the height range from 3 to 4 km during time period 3 and a warming of that layer during time period 5. Five-minute mean temperature data

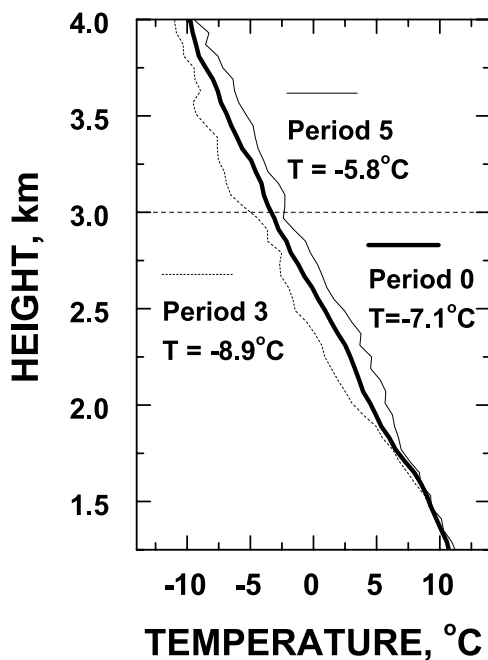


Figure 6. Five-minute mean temperature profiles for time intervals 3 (ascending phase, dashed line) and 5 (descending phase, thin line) in Figure 1 (evening) compared to the temperature profile for time interval 0 (before the arrival of the gravity wave, thick line). Mean temperature values for the 3- to 4-km layer are given.

above 4 km are not shown because they were rather noisy (strongly attenuated by clouds during period 5). The calculation of the 5-min mean relative humidity profiles, shown in Figure 7, is based on the 5-min mean mixing ratio profiles and the 35-min mean temperature profile (Figure 4) that was shifted by -0.3 K, -1.2 K, -1.8 K, -1.5 K, and $+1.3$ K for the time periods 1–5, respectively. The temperature shift corresponds to the mean lifting

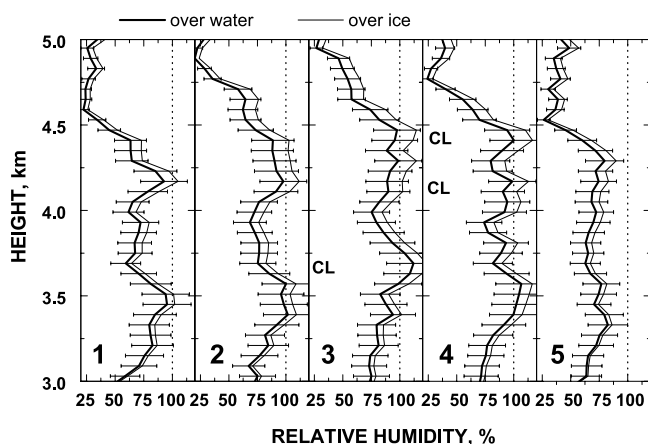


Figure 7. Relative humidity profiles for the time intervals 1–5 in Figure 1 (evening) calculated from measured 5-min mixing ratio profiles (180-m signal smoothing) and estimated 5-min temperature profiles. Beginning of cloud formation is indicated by CL. Error bars include statistical and systematic errors.

height for each of the periods 1–5 by assuming adiabatic conditions.

[27] As can be seen in Figure 7, all clouds obviously formed when the relative humidity reached 100% with respect to water (time periods 3 and 4). Because of the limited vertical resolution of 180 m in the case of the mixing ratio, peak humidity values that might have been present and were presumably responsible for the generation of the thin cloud layers could not be resolved. Ice supersaturation was close to 20% according to the lidar observations in the three clouds. The optical depth of the uppermost of the three clouds was about 0.2.

[28] During the descent phase of the gravity wave the clouds dissolved. Relative humidity decreased and was found below ice saturation at all heights in time period 5. Compared to profile 1, the water vapor distribution was almost homogeneous over the height range from 3.2 to 4.3 km, obviously as a result of evaporation of the cloud particles and turbulent mixing.

[29] The depolarization ratios in Figure 8 clearly show that the cloud particles were spherical and thus obviously liquid. Molecules cause depolarization ratios of about 0.015. The dust layers produced total depolarization ratios of 0.04–0.07. However, in the clouds, backscattering by molecules and dust is negligible and the depolarization ratio is determined by cloud particle backscattering. Spherical particles do not depolarize light at 180° scattering angle. The observed small depolarization ratio of 0.015 in the clouds is caused by scattering at angles $<180^\circ$ as a result of multiple scattering processes (several forward scattering processes and one backscattering process [Wandinger, 1998]). This behavior of weak cloud depolarization was found throughout the lifetime of all three cloud layers. In contrast to spherical drops, nonspherical ice crystals produce significant depolarization by internal reflections within each of the crystals. Several depolarizing (non- 180°) scattering events

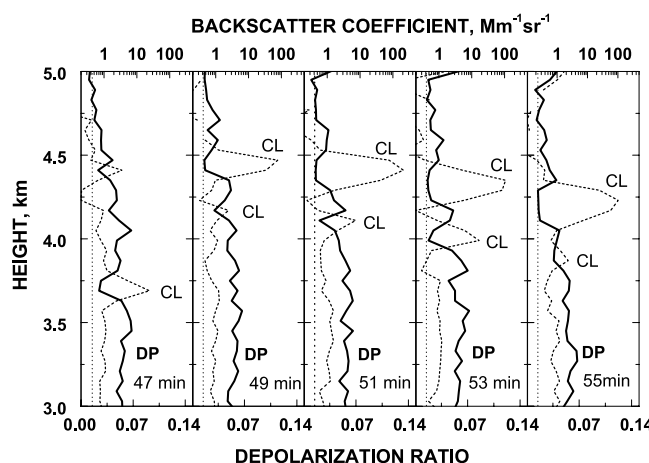


Figure 8. Total depolarization ratio (thick line) and particle backscatter coefficient (dashed line). CL indicates cloud. The strong decrease of the depolarization ratio in the presence of clouds results from backscattering by spheres. The dotted vertical line indicates 1.5% depolarization ratio. For comparison with Figure 1 (evening), time after start of measurement is given.

take place in crystals, finally adding up to a 180° scattering process [Sassen, 1991].

[30] Because no evidence for significant ice production was observed, we assume that most of the aged dust particles were partly coated with hygroscopic substances in the cloud layer, thus deactivated (concerning ice initiation), and acted as condensation nuclei to form a high number of comparably small liquid drops when the relative humidity exceeded the water saturation level. Temperatures were then obviously too high to initiate freezing (deposition freezing, condensation/immersion freezing) in the next step. On the other hand, although the meteorological conditions for contact freezing were favorable, the number of remaining dust particles (ice nuclei) may have been too small to produce a significant, detectable amount of ice by this mechanism. It is also possible that the cloud drops were too small. As pointed out by Young [1974] contact freezing efficiency also depends on the size of the liquid drops. The efficiency decreases with decreasing cloud drop size.

[31] Nevertheless, the result is surprising. The upper two clouds (below 5-km height) formed in the wave crest and persisted in the descending branch of the wave. As found in previous studies [e.g., Young, 1974; Field *et al.*, 2001; Cotton and Field, 2002] one would expect that the cloud particles nucleate in the wave crest when the water saturation level is reached and then quickly glaciates (even in the absence of desert dust) such that the ice particles only evaporate when the descending air reaches ice subsaturation again. Contact freezing is noted to be suppressed in updrafts and enhanced during the downward motion phase as a result of enhanced turbulent mixing in evaporation zones [Young, 1974].

[32] It should be mentioned however that we cannot conclude from the depolarization measurements that ice crystals were absolutely absent because the impact of a few ice crystals on the depolarization ratio would not be resolvable. However, specular reflection resulting from strong backscattering by falling, horizontally oriented ice crystals that also leads to very low depolarization ratios [Thomas *et al.*, 1990; Noel and Sassen, 2004] can be excluded. There is no hint on sedimentation processes. The cloud parcels almost perfectly followed the main air flow forced by the gravity wave. Estimates of the 532-nm extinction coefficient of $1000\text{--}1500\text{ Mm}^{-1}$ (180-m signal smoothing) in the uppermost of the three clouds indicate dominant light scattering by liquid water drops.

4.3. Glaciating Altocumulus Clouds

[33] A detailed analysis of the humidity conditions in the altocumulus layer observed during the afternoon of 21 November 2003, was not possible. Water vapor Raman signals are too weak at daytime to allow the determination of trustworthy humidity profiles at the 6-km height level. As outlined in section 4.1, temperatures ranged from -18°C at 5150-m height to -27°C at 6300-m height.

[34] The afternoon observation of the depolarization ratio is presented in Figure 9. In terms of particle depolarization the broken cloud field is characterized by a dark blue band reflecting the presence of liquid drops in the center region of the cloud. Air parcels with ice crystals were identified by high depolarization at the cloud rims (red spots in Figure 9 between 5- and 6.5-km height). No sign of ice formation

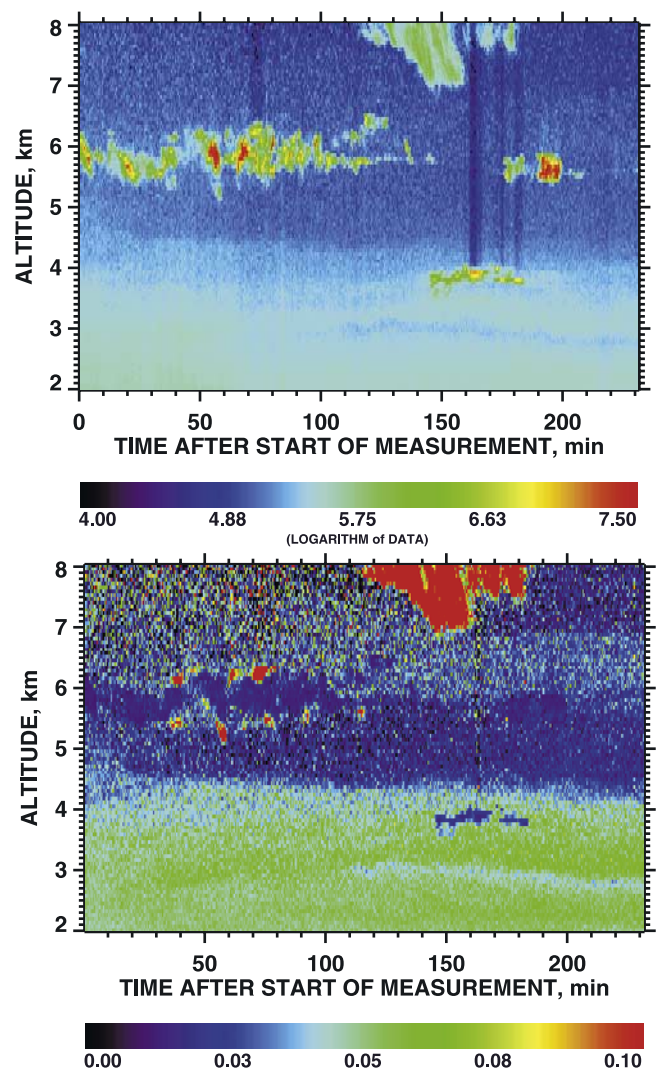


Figure 9. (top) Range-corrected 532-nm signal and (bottom) total depolarization ratio observed during the afternoon of 21 November 2003 (1212–1600 UTC). Altocumulus was observed between 5- and 6.5-km height and at 4-km height. The dark blue band in Figure 9 (bottom) up to minute 120 after measurement start indicates drops in the cloud center layer. Red spots indicate ice crystals at the cloud rims. Light blue and green in Figure 9 (bottom) indicate dust.

was found in the clouds detected at 4 and 5.7-km height 140–200 min after start of measurement.

[35] The rather constant depolarization ratio of 0.015–0.025 in the center of the altocumulus layer (dark blue band) suggests that horizontally aligned, falling ice crystals were absent in this region. This hypothesis is corroborated by the fact that pronounced descending layers were not observed. Furthermore, the estimated cloud mean lidar ratio of 20 sr (see section 4.1) indicates drops. Falling, horizontally oriented ice crystals lead to lidar ratios of <5 sr [Ansmann *et al.*, 1992; Reichardt *et al.*, 2002] as mentioned above.

[36] Note that depolarization ratios of the order of 0.1 (red spots in Figure 9) can also be caused by spherical particles, but only in the case of strong multiple scattering in dense

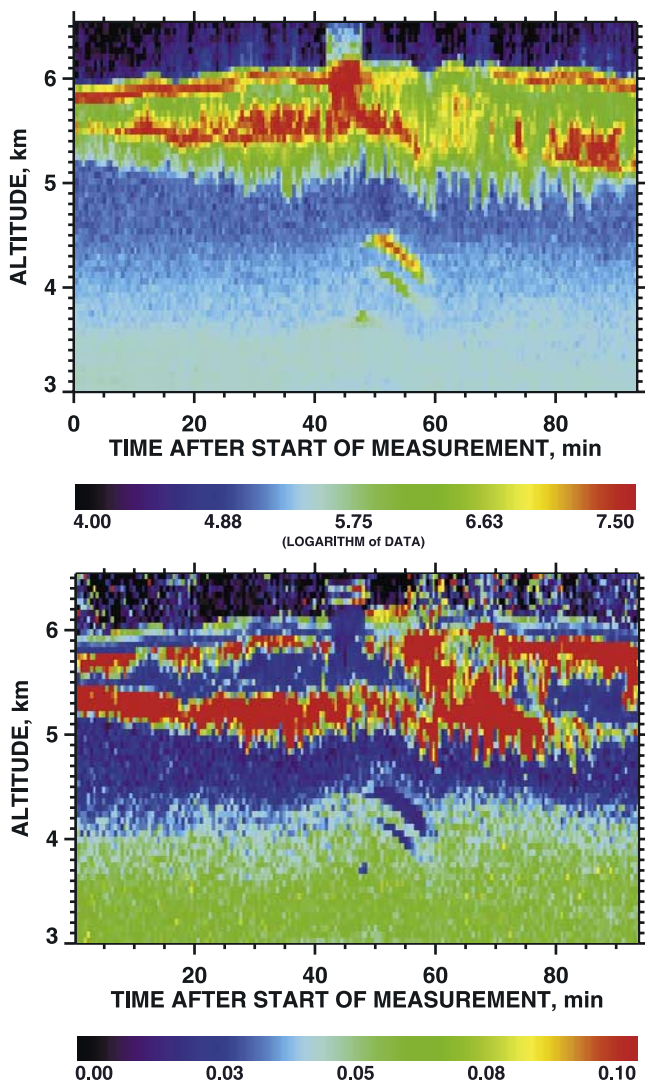


Figure 10. (top) Range-corrected 532-nm signal and (bottom) total depolarization ratio observed during the evening of 21 November 2003 (1627–1800 UTC). An altocumulus layer was present above 5-km height. Gravity-wave-induced clouds formed below 4.5-km height. In Figure 10 (bottom), blue or blue colors at the top of the altocumulus layer and in the gravity wave clouds indicate liquid water drops. Green to red in the altocumulus (below the liquid water layer) indicate randomly oriented ice crystals, blue in the cloud center indicates horizontally aligned ice crystals. Maximum depolarization ratios were close to 0.14.

water clouds with optical depths >1 [Wandinger, 1998]. It is therefore unlikely that multiple scattering by drops contributed to the observed depolarization ratios of 0.1–0.15 at the cloud edges because the optical depths of the respective cloud parcels were much too low (of the order of 0.05–0.1). Furthermore, multiple scattering typically causes a monotonic and smooth increase of the depolarization ratio with penetration depth of the laser light into the cloud instead of the observed strong depolarization variations with height.

[37] Because temperatures were between -19°C and -27°C (see Figure 3), condensation/immersion freezing and deposition freezing may have contributed to the

observed ice formation. However, the detected features (no ice in the cloud interior and ice near the cloud edges) corroborate the hypothesis that contact freezing played an important role [Young, 1974]. Contact freezing preferably occurs in zones of evaporation, when, e.g., dry, subsaturated air is mixed with cloud air.

[38] Figure 10 shows the observation of the well-developed cloud deck in the evening of 21 November 2003. The thin liquid water layer at cloud top caused very low depolarization ratios. The slightly enhanced depolarization ratio values at the top of the thin, optically dense liquid water layer is most probably caused by multiple scattering. Before the passage of the strong gravity wave, ice crystals must have formed in and just below the liquid water layer. Depolarization by ice crystal backscatter in the liquid water layer is obscured by the dominant nonpolarizing backscattering by drops. The crystals grew and began to fall. After the initial sedimentation phase (indicated by a layer of enhanced depolarization below the liquid water layer, red in Figure 10) they were aligned horizontally so that the depolarization ratio decreased again to very low values. Our lidar ratio observation corroborate the interpretation of aligned crystals in the central part of the cloud. Lidar ratios were mainly close to 1–2 sr, a clear sign of horizontally aligned crystals (see Figure 4b).

[39] Below about 5.5 km the crystals began to evaporate. According to Figure 5, the relative humidity over ice was below 100% at that altitude. The crystals became small again and most of them were no longer able to keep their horizontal orientation. As pointed out by Sassen [1980] random orientation also dominates during falling if the maximum dimension of the crystals is less than about $100\ \mu\text{m}$. The depolarization ratio increased again to values of 0.1–0.15 in the lower part of the cloud. Evaporation humidified the lower cloud region so that subsequent crystal virga could reach lower and lower heights. The increase of the lidar ratio toward values of 10 sr at cloud base (see Figure 4) also indicates that the number of randomly oriented crystals steadily increased from cloud center to cloud bottom.

[40] Liquid droplets may also have contributed to the very low depolarization values in the cloud center region. However, if only a few crystals are present in the beginning of an ice formation process these few crystals will grow rapidly at the expense of the liquid water drops and will cause the drops to shrink and to dissolve with time because the relative humidity over water is significantly lower than over ice.

[41] The depolarization ratios of 0.1–0.15 observed in the lower part of the cloud deck indicate plate-like crystals [Reichardt *et al.*, 2002] taking into account that always a few crystals causing specular reflection are present and may cause a 20–50% reduction of the depolarization ratio in the case of a vertically pointing lidar [Noel and Sassen, 2004] compared to the case of an off-zenith pointing lidar. Model calculations yield depolarization ratios of 0.2–0.3 for plates [Reichardt *et al.*, 2002]. In contrast, columns produce much higher depolarization ratios of ≥ 0.5 .

[42] Hogan *et al.* [2003a] observed a similar altocumulus evolution over Chilbolton, United Kingdom, in October 1998. The cloud formed between 4.5- and 6.5-km height in a southwesterly air flow in the absence of desert dust. An airborne lidar detected a highly reflecting 150-m-thick liquid water layer with an optical depth of >0.7 at cloud

top. The depolarization ratio was close to 0.02 in the liquid water layer. Ice crystal fall streaks beneath that thin layer produced depolarization ratios of 0.1–0.15.

[43] Such a layering with a thin liquid layer at the top of the cloud deck and extended ice particle fall streaks occurs in many altocumulus clouds [Hogan *et al.*, 2003b]. Under background conditions in the free troposphere the IN concentration is $<0.01\text{--}0.03\text{ cm}^{-3}$ and can be of the order of 1 cm^{-3} in desert dust layers, as observed in Saharan dust several thousands of kilometers away from the source region [DeMott *et al.*, 2003]. The presence of desert dust thus certainly led to a largely increased ice formation (large number of ice crystals) because of the largely enhanced number of available ice nuclei.

[44] An interesting feature was observed when the gravity wave crossed the field site. During the lifting phase (see Figure 10, minutes 40–50) the sandwich-like depolarization structure of the cloud became significantly disturbed. In the upper part of the cloud strong scattering by liquid particles appeared, the depolarization ratio dropped to values close to zero. As can be seen in Figure 5, after the ascent of the air parcels by 250 m, water supersaturation must have prevailed above 5.7-km height so that the existing drops became significantly larger and new drops may have formed. The drops determined the depolarization ratio even if ice crystals were present in the upper part of the cloud. Since ice supersaturation is close to 35% when water saturation is reached at about -20°C , conditions were rather favorable for strong ice formation by contact freezing at cloud top during the downdraft (region of water subsaturation). Contact freezing was further favored because of the large number of large drops after the ascent of the cloud parcels [Young, 1974]. Ice formation by condensation, immersion and deposition freezing can also take place at these meteorological conditions.

[45] The enhanced backscattering and depolarization above the top of the cloud (visible in Figure 10 above 6.2-km height, 40–50 min after measurement start), when the wave crest crossed the field site, is an artifact, most probably caused by strong multiple scattering. The multiply (forward) scattered light is backscattered much later than the respective light backscattered from cloud top (before and after the event), so that the received signal is interpreted as light backscattered from greater heights.

[46] The abrupt change in the depolarization characteristics in the upper part of the altocumulus (see Figure 10, minute 47) marks the beginning of strong ice formation during the downdraft when the air was water subsaturated. The depolarization ratio remained high (red in Figure 10) during falling of the crystals through the cloud. The ice crystals may have been too small for horizontal alignment or turbulent mixing prevented the horizontal alignment of crystals during falling. It is expected that the high number of available IN caused the formation of a comparably large number of relatively small ice crystals. After the passage of the gravity wave, the cloud system recovered and returned to the sandwich-like structures.

[47] It is interesting to note that aircraft in situ observations of an isolated stationary gravity wave cloud over Scandinavia in October 1999 [Cotton and Field, 2002] are consistent with our findings although the measured IN concentration of $<0.01\text{ cm}^{-3}$ indicated aerosol background conditions (no dust). During the ascent phase after the formation of drops

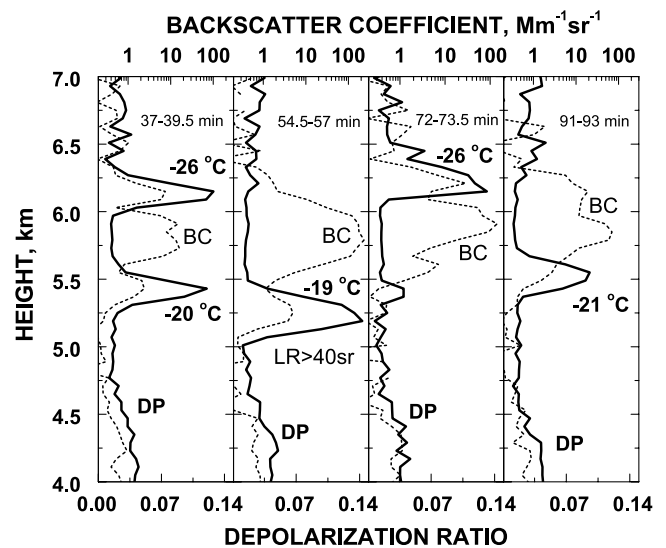


Figure 11. Total depolarization ratio (thick line) and particle backscatter coefficient (dashed line) in the altocumulus layer observed in the afternoon (see Figure 9). Temperatures are given for the depolarization peak heights. For comparison with Figure 9, time period after measurement start is given. In one of the ice crystal layers an extinction-to-backscatter ratio LR of 40–45 sr could be determined.

(200 cm^{-3}), the drop concentration remained constant during further lifting while the water content increased and reached a maximum at the updraft-downdraft boundary. During the downdraft, the dominant phase of the cloud changed from liquid to ice and the particle number concentration fell rapidly to 10 cm^{-3} in the water-subsaturated environment. The ice crystals had maximum sizes (diameters) of $300\text{ }\mu\text{m}$. A few ice crystals were already formed in the liquid water region (before the phase transition).

[48] Finally, we briefly discuss the shape characteristics of crystals formed on dust particles. According to Bailey and Hallett [2002] dust-induced ice formation typically leads to incomplete plate-like crystals and irregularly shaped polycrystals consisting of plate-like crystals. It is known from model calculations that the backscatter coefficient of irregularly shaped, randomly oriented crystals can be less by up to an order of magnitude compared to the respective backscatter coefficients of perfectly formed hexagonal ice crystals [Macke, 1993; Reichardt *et al.*, 2002]. As a consequence the lidar ratio of irregularly shaped crystals is significantly increased. Perfectly formed small hexagonal plates and columns in upper tropospheric cirrus typically produce values of 10–20 sr. In one of the glaciating cloud parcels in Figure 11, the lidar ratio could be determined and showed a comparably high value of 40–45 sr. The result of Bailey and Hallett [2002] is further corroborated by the fact that the peak depolarization ratios in Figure 11 also indicate plates, as discussed above.

5. Summary

[49] For the first time, ice formation in midtropospheric clouds embedded in a Saharan dust layer was studied in

detail on the basis of Raman lidar observations of dust and cloud optical properties, temperature, and relative humidity. Three gravity-wave-induced clouds and another cloud layer at about 4-km height did not show any sign of ice formations. Cloud temperatures ranged from -9 to -16°C . It was concluded that the aged dust below 4.5-km height was partly coated with hygroscopic material and thus deactivated.

[50] In the altocumulus layers, ice formation was observed at temperatures about 10–20 K higher than the temperatures at which ice formation in the absence of insoluble particles occurs. A gravity wave lifted the altocumulus layer by about 250 m and triggered intensive ice formation during the downdraft. The observation of ice formation at cloud edges and in downdraft region suggests that contact freezing played a major role in the ice formation process.

[51] From the lidar observations one may conclude that a proper modeling of the indirect effect of desert dust requires a good knowledge of the transport way of the dust. Aged dust in the lower free troposphere may be deactivated by anthropogenic emissions and as a result of mixing with hygroscopic particles so that ice formation is strongly suppressed in respective dust layers. Dust particles that are lifted already in the source region to heights above 4 km and transported at heights >4 km height may preserve their ice nuclei properties even after a transport of several thousands of kilometers so that they can effectively influence ice formation in clouds far away from desert regions.

[52] As demonstrated, advanced Raman lidars can significantly contribute to cloud research. Long-term lidar observations may help to better understand the dust impact on cloud formation by contrasting dust-free and dust outbreak cases. On the basis of long-term monitoring with lidar it may also be possible to better characterize the relative importance of the different ice formation mechanisms concerning freezing of water clouds in the lower and middle troposphere as a function of meteorological condition (including air mass transport pattern) and dust properties (young and aged dust, contaminated dust).

[53] **Acknowledgments.** We are grateful to the Meteorological Observatory Lindenberg for kindly providing the five-point surface pressure observations. We thank the reviewers for their fruitful comments.

References

- Ansmann, A. (2002), Molecular-backscatter lidar profiling of the volume-scattering coefficient in cirrus, in *Cirrus*, edited by D. K. Lynch, K. Sassen, D. O'C. Starr, and G. Stephens, pp. 197–210, Oxford Univ. Press, New York.
- Ansmann, A., M. Riebesell, and C. Weitkamp (1990), Measurement of atmospheric aerosol extinction profiles with a Raman lidar, *Opt. Lett.*, **15**, 746–748.
- Ansmann, A., U. Wandinger, M. Riebesell, C. Weitkamp, and W. Michaelis (1992), Independent measurement of extinction and backscatter profiles in cirrus clouds by using a combined Raman elastic-backscatter lidar, *Appl. Opt.*, **31**, 7113–7131.
- Ansmann, A., et al. (2003), Long-range transport of Saharan dust to northern Europe: The 11–16 October 2001 outbreak observed with EARLINET, *J. Geophys. Res.*, **108**(D24), 4783, doi:10.1029/2003JD003757.
- Arshinov, Y., S. Bobrovnikov, I. Serikov, A. Ansmann, D. Althausen, I. Mattis, and U. Wandinger (2001), Spectrally absolute instrumental approach to isolate pure rotational Raman lidar returns from nitrogen molecules of the atmosphere, in *Advances in Laser Remote Sensing*, edited by A. Dabas, C. Loth, and J. Pelon, pp. 121–124, Ecole Polytech., Palaiseau, France.
- Bailey, M., and J. Hallett (2002), Nucleation effects on the habit of vapour grown ice crystals from -18 to -42°C , *Q. J. R. Meteorol. Soc.*, **128**, 1461–1483.
- Bösenberg, J., et al. (2003), EARLINET: A European Aerosol Research Lidar Network to establish an aerosol climatology, *MPI Rep. 343*, Max-Planck-Institut für Meteorol., Hamburg, Germany.
- Bobrovnikov, S. M., Y. F. Arshinov, I. B. Serikov, D. Althausen, A. Ansmann, I. Mattis, and U. Wandinger (2002), Daytime temperature profiling in the troposphere with a pure rotational Raman lidar, in *Laser Remote Sensing in Atmospheric and Earth Sciences, Proceedings of the 21st International Laser Radar Conference, Quebec City, Canada*, edited by L. R. Bissonnette, G. Roy, and G. Vallée, pp. 717–720, Def. R&D Can.-Valcartier, Val-Bélair, Quebec, Canada.
- Cotton, R. J., and P. R. Field (2002), Ice nucleation characteristics of an isolated wave cloud, *Q. J. R. Meteorol. Soc.*, **128**, 2417–2437.
- DeMott, P. J. (2002), Laboratory studies of cirrus cloud processes, in *Cirrus*, edited by D. K. Lynch, K. Sassen, D. O'C. Starr, and G. Stephens, pp. 102–135, Oxford Univ. Press, New York.
- DeMott, P. J., D. C. Rogers, and S. M. Kreidenweis (1997), The susceptibility of ice formation in upper tropospheric clouds to insoluble aerosol components, *J. Geophys. Res.*, **102**, 19,575–19,584.
- DeMott, P. J., K. Sassen, M. R. Poellot, D. Baumgardner, D. C. Rogers, S. D. Brooks, A. J. Prenni, and S. M. Kreidenweis (2003), African dust aerosols as atmospheric ice nuclei, *Geophys. Res. Lett.*, **30**(14), 1732, doi:10.1029/2003GL017410.
- European Centre for Medium-Range Weather Forecasts (ECMWF) (1995), User guide to ECMWF products 2.1, *Meteorol. Bull. M3.2*, Reading, UK.
- Field, P. R., et al. (2001), Ice nucleation in orographic wave clouds: Measurements made during INTACC, *Q. J. R. Meteorol. Soc.*, **127**, 1493–1512.
- Hoffer, T. E. (1961), A laboratory investigation of droplet freezing, *J. Meteorol.*, **18**, 766–778.
- Hogan, R. J., P. N. Francis, H. Flentje, A. J. Illingworth, M. Quante, and J. Pelon (2003a), Characteristics of mixed-phase clouds. I: Lidar, radar and aircraft observations from CLARE'98, *Q. J. R. Meteorol. Soc.*, **129**, 2089–2116.
- Hogan, R. J., A. J. Illingworth, E. J. O'Connor, and J. P. V. Póiares Baptista (2003b), Characteristics of mixed-phase clouds. II: A climatology from ground-based lidar, *Q. J. R. Meteorol. Soc.*, **129**, 2117–2134.
- Isono, K., M. Komabayasi, and A. Ono (1959), The nature and the origin of ice nuclei in the atmosphere, *J. Meteorol. Soc. Jpn.*, **37**, 211–233.
- Macke, A. (1993), Scattering of light by polyhedral ice crystals, *Appl. Opt.*, **32**, 2780–2788.
- Mason, B. J. (1960), Ice-nucleating properties of clay materials and stony meteorites, *Q. J. R. Meteorol. Soc.*, **86**, 552–556.
- Mason, B. J., and J. Maybank (1958), Ice-nucleating properties of some natural mineral dusts, *Q. J. R. Meteorol. Soc.*, **84**, 235–241.
- Mattis, I. (2002), Aufbau eines Feuchte-Temperatur-Aerosol-Ramanlidars und Methodenentwicklung zur kombinierten Analyse von Trajektorien und Aerosolprofilen (Development of a humidity/temperature/aerosol Raman lidar and of methods for the combined analysis of backward trajectories and aerosol profiles), Ph.D. thesis, 134 pp., Univ. Leipzig, Leipzig, Germany.
- Mattis, I., A. Ansmann, D. Althausen, V. Jaenisch, U. Wandinger, D. Müller, Y. F. Arshinov, S. M. Bobrovnikov, and I. B. Serikov (2002a), Relative-humidity profiling in the troposphere with a Raman lidar, *Appl. Opt.*, **41**, 6451–6462.
- Mattis, I., A. Ansmann, D. Müller, U. Wandinger, and D. Althausen (2002b), Dual-wavelength Raman lidar observations of the extinction-to-backscatter ratio of Saharan dust, *Geophys. Res. Lett.*, **29**(9), 1306, doi:10.1029/2002GL014721.
- Mattis, I., A. Ansmann, D. Müller, U. Wandinger, and D. Althausen (2004), Multiyear aerosol observations with dual-wavelength Raman lidar in the framework of EARLINET, *J. Geophys. Res.*, **109**, D13203, doi:10.1029/2004JD004600.
- Müller, D., I. Mattis, U. Wandinger, A. Ansmann, D. Althausen, O. Dubovik, S. Eckhardt, and A. Stohl (2003), Saharan dust over a central European EARLINET-AERONET site: Combined observations with Raman lidar and Sun photometer, *J. Geophys. Res.*, **108**(D12), 4345, doi:10.1029/2002JD002918.
- Noel, V., and K. Sassen (2004), Study of ice crystal orientation in ice clouds based on polarized observations from the FARS scanning lidar, in *Reviewed and Revised Papers Presented at the 22nd International Laser Radar Conference (ILRC 2004), 12–16 July 2004, Matera, Italy*, edited by G. Pappalardo and A. Amodeo, *Eur. Space Agency Spec. Publ., ESA SP-561*, 309–312.
- O'Connor, E. J., A. J. Illingworth, and R. J. Hogan (2004), A technique for autocalibration of cloud lidar, *J. Atmos. Oceanic Technol.*, **21**, 777–786.
- Pitter, R. L., and H. R. Pruppacher (1973), A wind tunnel investigation of freezing of small water drops falling at terminal velocity in air, *Q. J. R. Meteorol. Soc.*, **99**, 540–550.

- Pruppacher, H. R., and J. D. Klett (1997), *Microphysics of Clouds and Precipitation*, 954 pp., Springer, New York.
- Reichardt, J., S. Reichardt, M. Hess, and T. J. McGee (2002), Correlations among the optical properties of cirrus-cloud particles: Microphysical interpretation, *J. Geophys. Res.*, *107*(D21), 4562, doi:10.1029/2002JD002589.
- Roberts, P., and J. Hallett (1968), A laboratory study of the ice nucleating properties of some mineral particulates, *Q. J. R. Meteorol. Soc.*, *94*, 25–34.
- Sakai, T., T. Nagai, M. Nakazato, and T. Matsumura (2003), Ice clouds and Asian dust studied with lidar measurements of particle extinction-to-backscatter ratio, particle depolarization, and water vapor mixing ratio over Tsukuba, *Appl. Opt.*, *42*, 7103–7116.
- Sakai, T., T. Nagai, M. Nakazato, and T. Matsumura (2004), Raman lidar measurement of water vapor and ice clouds associated with Asian dust layer over Tsukuba, Japan, *Geophys. Res. Lett.*, *31*, L06128, doi:10.1029/2003GL019332.
- Sassen, K. (1980), Remote sensing of planar ice crystal fall attitudes: A model study of the homogeneous and heterogeneous modes, *J. Meteorol. Soc. Jpn.*, *58*, 422–429.
- Sassen, K. (1991), The polarization lidar technique for cloud research: A review and current assessment, *Bull. Am. Meteorol. Soc.*, *72*, 1848–1866.
- Sassen, K. (2002), Indirect climate forcing over the western US from Asian dust storms, *Geophys. Res. Lett.*, *29*(10), 1465, doi:10.1029/2001GL014051.
- Sassen, K., and S. Benson (2000), Ice nucleation in cirrus clouds: A model study of the homogeneous and heterogeneous modes, *Geophys. Res. Lett.*, *27*, 521–524.
- Sassen, K., P. J. DeMott, J. M. Prospero, and M. R. Poellot (2003), Saharan dust storms and indirect aerosol effects on clouds: CRYSTAL-FACE results, *Geophys. Res. Lett.*, *30*(12), 1633, doi:10.1029/2003GL017371.
- Schaller, R. C., and N. Fukuta (1979), Ice nucleation by aerosol particles: Experimental studies using a wedge-shaped ice thermal diffusion chamber, *J. Atmos. Sci.*, *36*, 1788–1802.
- Stohl, A., G. Wotawa, P. Seibert, and H. Kromp-Kolb (1995), Interpolation errors in wind fields as a function of spatial and temporal resolution and their impact on different types of kinematic trajectories, *J. Appl. Meteorol.*, *34*, 2149–2165.
- Tegen, I., M. Werner, S. P. Harrison, and K. E. Kohfeld (2004), Relative importance of climate and land use in determining present and future global soil dust emission, *Geophys. Res. Lett.*, *31*, L05105, doi:10.1029/2003GL019216.
- Thomas, L., J. C. Cartwright, and D. P. Wareing (1990), Lidar observations of the horizontal orientation of ice crystals in cirrus clouds, *Tellus, Ser. B*, *42*, 211–216.
- Wandinger, U. (1998), Multiple-scattering influence on extinction- and backscatter-coefficient measurements with Raman and high-spectral-resolution lidars, *Appl. Opt.*, *37*, 417–427.
- Young, K. C. (1974), The role of contact nucleation in ice phase initiation in clouds, *J. Atmos. Sci.*, *31*, 768–776.
- Zuberi, B., A. K. Bertram, C. A. Cassa, L. T. Molina, and M. J. Molina (2002), Heterogeneous nucleation of ice in $(\text{NH}_4)_2\text{SO}_4\text{-H}_2\text{O}$ particles with mineral dust immersions, *Geophys. Res. Lett.*, *29*(10), 1504, doi:10.1029/2001GL014289.
-
- D. Althausen, A. Ansmann, I. Mattis, D. Müller, M. Radlach, and U. Wandinger, Leibniz Institute for Tropospheric Research, Permoserstr. 15, D-04318 Leipzig, Germany. (detlef@tropos.de; albert.ansmann@tropos.de; ina@tropos.de; dietrich@tropos.de; radlach@tropos.de; ulla@tropos.de)
- R. Damoah, Technische Universität München, Am Hochanger 13, D-85354 Freising-Weihenstephan, Germany. (damoah@forst.tu-muenchen.de)